Energy Materials

Article

Porous Nb$_4$W$_7$O$_{31}$ microspheres with a mixed crystal structure for high-performance Li+ storage

Xingxing Jin[1,#], Qiang Yuan[1,#], Xiaolin Sun[2,3,4,#], Xuehua Liu[1], Jianfei Wu[2,3,4,*] (iD), Chunfu Lin[1,*] (iD)

[1]Institute of Materials for Energy and Environment, College of Materials Science and Engineering, Qingdao University, Qingdao 266071, Shandong, China.
[2]Qingdao Institute of Bioenergy and Bioprocess Technology, Chinese Academy of Sciences, Qingdao 266101, Shandong, China.
[3]Shandong Energy Institute, Qingdao 266101, Shandong, China.
[4]Qingdao New Energy Shandong Laboratory, Qingdao 266101, Shandong, China.
[#]Authors contributed equally.

Correspondence to: Prof./Dr. Chunfu Lin, Institute of Materials for Energy and Environment, College of Materials Science and Engineering, Qingdao University, 308 Ningxia Road, Qingdao 266071, Shandong, China. E-mail: linchunfu@qdu.edu.cn; Prof./Dr. Jianfei Wu, Qingdao Institute of Bioenergy and Bioprocess Technology, Chinese Academy of Sciences, 189 Songling Road, Qingdao 266101, Shandong, China; Shandong Energy Institute, 189 Songling Road, Qingdao 266101, Shandong, China; Qingdao New Energy Shandong Laboratory, 189 Songling Road, Qingdao 266101, Shandong, China. E-mail: wujf@qibebt.ac.cn

Abstract

Niobium-tungsten oxides with tungsten bronze and confined ReO$_3$ crystal structures are prospective anode candidates for lithium-ion batteries since the multi-electron transfer *per* niobium/tungsten offers large specific capacities. To combine the merits of the two structures, porous Nb$_4$W$_7$O$_{31}$ microspheres constructed by nanorods are synthesized based on a facile solvothermal method. This new material contains different tungsten bronze structures and 4 × 4 ReO$_3$-type blocks confined by tungsten bronze matrices, generating plenty of pentagonal and quadrangular tunnels for Li+ storage, as confirmed by spherical-aberration-corrected scanning transmission electron microscopy. Such structural mixing enables three-dimensionally uniform and small lattice expansion/shrinkage during lithiation/delithiation, leading to good structural and cyclic stability (95.2% capacity retention over 1,500 cycles at 10C). The large interlayer spacing (~3.95 Å), coupled with the abundant pentagonal/quadrangular tunnels, results in ultra-high Li+ diffusion coefficients (1.24 × 10^{-11} cm^2 s^{-1} during lithiation and 1.09 × 10^{-10} cm^2 s^{-1} during delithiation) and high rate capability (10C *vs.* 0.1C capacity retention percentage of 47.6%). Nb$_4$W$_7$O$_{31}$ further exhibits a large reversible capacity (252 mAh g^{-1} at 0.1C), high first-cycle Coulombic efficiency (88.4% at 0.1C), and safe operating potential (~1.66 V *vs.* Li/Li+). This comprehensive study demonstrates that the porous Nb$_4$W$_7$O$_{31}$ microspheres are very promising anode materials for future use in high-performance Li +storage.

INTRODUCTION

Lithium-ion batteries (LIBs), as typical representatives of secondary batteries, have dominated power sources for consumable electronics[1-5]. To satisfy the booming development need for electric vehicles, the exploration of high-performance Li^+-storage materials with high reversible capacities, safe operation, superior rate capabilities, excellent cyclic stability, and high first-cycle Coulombic efficiencies is highly necessary. As for the anode materials, the intercalation type shows much better cyclic stability than the alloying and conversion types, being more practical for commercial LIBs[6]. At present, the most popular anode material is based on intercalation-type graphite owing to its large specific capacity (theoretically 372 mAh g^{-1}) and low cost. However, graphite faces a safety issue of lithium-dendrite formation when fast discharged/charged at its extremely low potential plateau (< 0.1 V *vs.* Li/Li^+)[7]. Intercalation-type $Li_4Ti_5O_{12}$, which is the second most popular anode material, exhibits a safe and flat potential plateau (~1.55 V), avoiding the above safety issue. Nevertheless, its theoretical capacity is insufficient (175 mAh g^{-1} within 1-3 V), hindering its appliance to some extent[8]. Hence, it is desirable to explore new, practical, and intercalation-type anode materials that simultaneously possess large reversible capacities and high safety performance.

Recently, niobium-tungsten oxide anode materials $Nb_{16}W_5O_{55}$ and $Nb_{18}W_{16}O_{93}$, with both large reversible capacities and high safety operation, were reported by Griffith *et al.*[5]. Owing to the redox couples Nb^{5+}/Nb^{4+}, Nb^{4+}/Nb^{3+}, W^{6+}/W^{5+}, and W^{5+}/W^{4+} with two-electron transfer *per* niobium/tungsten, these niobium-tungsten oxides show significantly larger theoretical/practical capacities than $Li_4Ti_5O_{12}$. Meanwhile, these four redox couples show safe operating potentials within 0.5-2.0 V, avoiding the lithium-dendrite formation and thus guaranteeing the safe operation. The niobium-tungsten oxides display open crystal structures[9-15], such as confined ReO_3 structures in $Nb_{16}W_5O_{55}$ and tetragonal tungsten bronze (TTB) structures in $Nb_{18}W_{16}O_{93}$, enabling fast Li^+ diffusivity for high rate performance. The 4 × 4 ReO_3-type blocks constructed by MO_6 octahedra (M = Nb/W) in $Nb_{16}W_5O_{55}$ are confined through edge sharing of some MO_6 octahedra and corner sharing of WO_4 tetrahedra, which guarantees good structural stability. The TTB structure is composed of pentagonal columns containing MO_7 pentagonal bipyramids by sharing equatorial edges with five MO_6 octahedra *per* bipyramid, linked in such a way that pentagonal, quadrangular, and triangular tunnels are formed. Compared to the confined ReO_3 structure, the TTB structure owns a larger interlayer spacing and numerous larger tunnels[16,17], which benefit Li^+ transport but harm structural stability. Therefore, it can be expected that niobium-tungsten oxide anode materials combining the above two structures can simultaneously have the merits of excellent structural robustness and superior Li^+ transport. Such niobium-tungsten oxide anode materials with mixed structures, however, have not been reported so far.

Here, porous $Nb_4W_7O_{31}$ microspheres with a mixed TTB and confined ReO_3 structure are synthesized based on a solvothermal process and applied as a new anode material for LIBs. The synthesis, crystal structures, electrochemical properties, and working mechanisms are systematically studied through various characterizations. As expected, this material exhibits superior Li^+ diffusion coefficients (D_{Li}) (1.24 × 10^{-11} cm^2 s^{-1} during lithiation and 1.09 × 10^{-10} cm^2 s^{-1} during delithiation), outstanding rate capability (10C *vs.* 0.1C capacity retention percentage of 47.6%), and excellent cyclic stability (95.2% capacity retention

after 1,500 cycles at 10C). Furthermore, it shows a large reversible capacity (252 mAh g^{-1} at 0.1C), high first-cycle Coulombic efficiency (88.4% at 0.1C), and safe operating potential (~1.66 V). During lithiation, external Li$^+$ ions are confirmed to be intercalated into the pentagonal and quadrangular tunnels of the mixed structure, homogeneously and slightly expanding the Nb$_4$W$_7$O$_{31}$ lattice in three dimensions, and this process is highly reversible.

RESULTS AND DISCUSSION

The reflections in the X-ray diffraction (XRD) pattern [Supplementary Figure 1] correspond to the characteristic peaks of Nb$_4$W$_7$O$_{31}$ (JCPDS 20-1320) except for three weak reflections belonging to tiny WO$_3$ impurity (JCPDS 43-1035). However, the crystal structure of Nb$_4$W$_7$O$_{31}$ has been in debate. The structure from JCPDS 20-1320, as proposed by N.C. Stephenson[18], is a TTB structure with the *P4* space group (Structure A, Figure 1A). It comprises NbO$_6$ and WO$_6$ octahedra in the Nb$_4$W$_7$O$_{31}$ framework with the characteristic of Nb/W mixed arrangement. The numbers of the pentagonal, quadrangular, and triangular prisms are 16, 9, and 16 *per* unit cell, respectively. A quarter of the pentagonal prisms are completely filled by the -O-Nb/W-O- strings, and 12 pentagonal tunnels, nine quadrangular tunnels, and 16 triangular tunnels [Supplementary Figure 2] in the overall cubic close-packed array are completely vacant. From the energy point of view, Structure B [Figure 1B], which is another TTB structure with filled pentagonal prisms at different positions, is also reasonable since the distance between the nearest filled pentagonal prisms (0.490*a*) is slightly larger than that in Structure A (0.486*a*). Additionally, Iijima proposed another reasonable structure for Nb$_4$W$_7$O$_{31}$ (Structure C, Figure 1C)[19]. A 4 × 4 ReO$_3$-type block in the middle of the unit cell is confined by a TTB-type matrix, resulting in abundant ion tunnels along the *c* direction. The numbers of the pentagonal, quadrangular, and triangular prisms are 12, 16, and 12, respectively, and a third of the pentagonal prisms are entirely filled by the -O-Nb/W-O- strings. It is known that the TTB structures tend to lose their stability when less than one-third of pentagonal prisms are filled[17]. Therefore, compared with Structure A and Structure B, Structure C is more stable. In addition, the total number of the large-sized pentagonal and quadrangular tunnels is larger (24 for Structure C *vs.* 21 for Structure A and Structure B), enabling faster Li$^+$ transport within the Nb$_4$W$_7$O$_{31}$ lattice. The XRD pattern is reasonably Rietveld-refined using a multiple-phase method (weighted profile residual: 9.08%)[20,21], showing that the mass percentages of Structure A, Structure B, and Structure C are 21.7(3), 22.1(3), and 56.2(2)%, respectively [Figure 1D]. The refined lattice constants are tabulated in Supplementary Table 1. It is noteworthy that the interlayer spacing of Nb$_4$W$_7$O$_{31}$ (equal to the *c* value) surpasses those of the reported niobate anode materials with confined ReO$_3$ and tungsten bronze structures [Supplementary Table 1], which undoubtedly benefits the Li$^+$ transport within the Nb$_4$W$_7$O$_{31}$ lattice.

The synthesized Nb$_4$W$_7$O$_{31}$ sample exhibits a porous-microspherical morphology with sphere diameters ranging from 2 μm to 7 μm [Figure 2A and B]. It is seen that nanorods with diameters between 20 nm and 100 nm and lengths between 60 nm and 1.5 μm are the primary building blocks, which are densely packed to form the porous microspheres [Supplementary Figure 3]. The heterogeneous distribution of nanorods with different sizes can enable a large tap density of the porous microspheres[22]. Each nanorod is a single crystal [Figure 2C] with its [001] crystal orientation along its longitudinal direction [Figure 2D]. The diffraction-spot deformation in the SAED pattern indicates the existence of abundant defects in the crystal, which is very reasonable since mixed crystal structures always contain defects. The energy-dispersive X-ray spectroscopy (EDX) mapping images in Figure 2E show that the Nb, W, and O elements are well dispersed throughout the tested porous microsphere. Figure 2F presents the N$_2$ adsorption-desorption isotherm of Nb$_4$W$_7$O$_{31}$, revealing its hierarchically porous characteristic with abundant pores centered at 3.8 and 71 nm [Figure 2F], which respectively correspond to the inter-rod and inter-sphere pores. The Branauer-Emmett-Teller (BET) specific surface area is calculated to be a large value of 11.4 m^2 g^{-1}. As a whole, the obtained
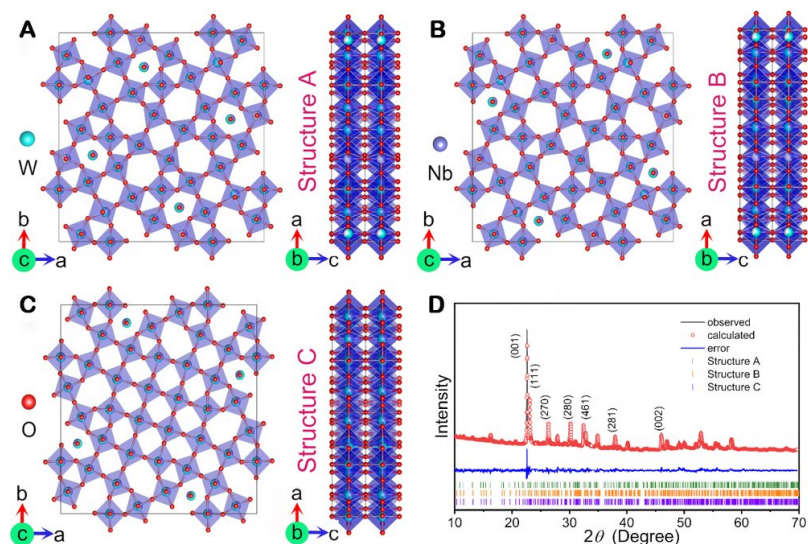
Figure 1. Crystal-structure units of $Nb_4W_7O_{31}$: (A) Structure A with a TTB type, (B) Structure B with another TTB type, and (C) Structure C with a confined ReO_3 type. (D) Rietveld-refined XRD pattern of $Nb_4W_7O_{31}$. The peaks of WO_3 at 23.8, 24.5, and 33.8° are removed during the refinement. For clarity, not all peaks of $Nb_4W_7O_{31}$ are indexed.
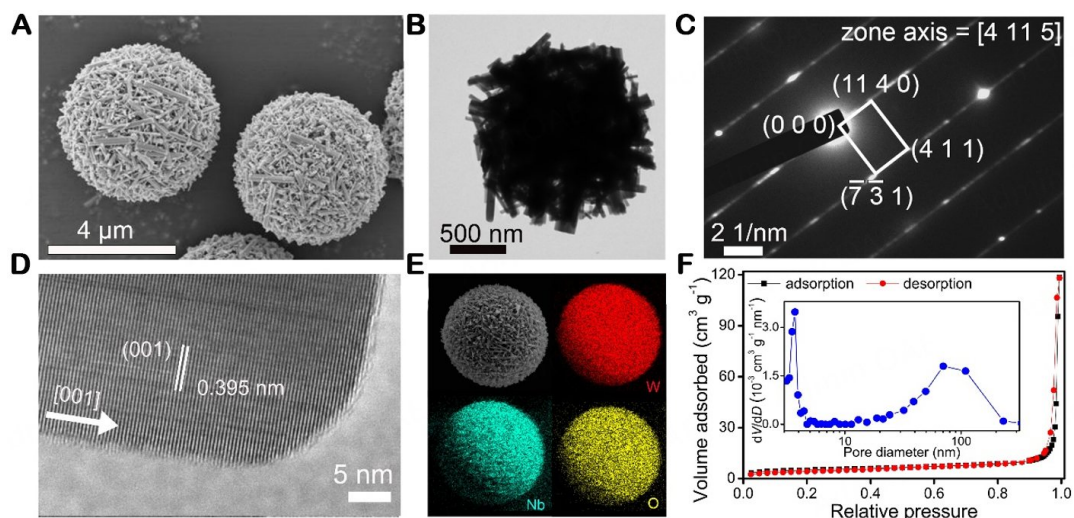
Figure 2. (A) FESEM image, (B) TEM image, (C) SAED pattern, (D) HRTEM image, (E) EDX mapping images, and (F) N_2 adsorption-desorption isotherm (*inset*: BJH pore-size distribution curve from desorption branch) of porous $Nb_4W_7O_{31}$ microspheres.

porous microspheres constructed by nanorods can offer fast electron transport along the nanorods, provide short Li^+ transport distances within the primary nanorods, give a large electrochemical-reaction area, enable easy electrolyte penetration, and guarantee a large tap density[23-27], being an ideal morphology for high-performance electrode materials.

To study the formation mechanism of the porous microspheres, three solvothermal experiments using different precursors are carried out [Supplementary Figure 4], and their final products are compared. First, when a precursor solution containing 0.86 mmol of $H_{28}N_6O_{41}W_{12}$ and 5.3 mmol of $NbCl_5$ dissolved in 60 mL isopropyl alcohol (IPA) is used, only nanoparticles can be found in the final product. Second, when 2 g tetrabutylammonium bromide (TBA) is added to the above precursor solution, only nanorods form. The

proper amount of TBA can selectively bind to the (001) oriented surfaces of the $Nb_4W_7O_{31}$ crystals, thus lowing the energy density of these surfaces and eventually guiding the growth of $Nb_4W_7O_{31}$ nanorods along the [001] crystal orientation[28]. Third, when 8 g hexadecyl trimethyl ammonium bromide (CTMAB) and 3 mL hydrochloric acid are further added into the precursor solution, the nanorods are self-assembled to yield hierarchical porous microspheres. This self-assembly process is accomplished with the aid of the CTMAB surfactant with a long, flexible, and non-branched hydrophobic chain[29]. CTMAB may modify the surface interaction between the $Nb_4W_7O_{31}$ nanorods and the acid solution, increasing the surface free energy of the nanorods as the liquid-solid phase separation proceeds, and thus favoring the self-assembly of nanorods into porous microspheres based on the lowest energy principle[30-32]. After this self-assembly, Ostwald ripening proceeds, during which large nanorods become larger while small nanorods become smaller in the porous microspheres. Clearly, the addition of TBA, CTMAB, and hydrochloric acid in proper amounts is the key to achieving the novel porous microspheres assembled by nanorods.

Figure 3A shows the galvanostatic discharge-charge curves of the $Nb_4W_7O_{31}$/Li half cell at current rates of 0.1C-10C (1C = 274 mA g^{-1}) in the potential window of 0.8-3.0 V. $Nb_4W_7O_{31}$ delivers a large first-cycle discharge/charge capacity of 285/252 mAh g^{-1} with a high Coulombic efficiency of 88.4% at 0.1C. The average operating potential is ~1.66 V during lithiation/delithiation, which is similar to those of the popular $Li_4Ti_5O_{12}$ and $TiNb_2O_7$ and suggests the high safety performance of $Nb_4W_7O_{31}$[8,33]. Each discharge/charge curve of $Nb_4W_7O_{31}$ presents two sloping regions and no plateaus, reflecting two solid-solution reactions throughout lithiation/delithiation, which is different from the two-phase-reaction involved behavior in $Li_4Ti_5O_{12}$ and $TiNb_2O_7$. The absence of two-phase reactions in $Nb_4W_7O_{31}$ is beneficial for its electrochemical kinetics since it is known that the Li$^+$ diffusion during two-phase reactions is relatively slow[34]. Additionally, the rate capability of $Nb_4W_7O_{31}$ is remarkable. With the current rate increasing, $Nb_4W_7O_{31}$ retains large reversible capacities of 235, 196, 171, 144, and 120 mAh g^{-1}, respectively at 0.5C, 1C, 2C, 5C, and 10C [Figure 3B]. As the current rate turns back to 0.5C, the capacity has no significant decay. Long-term cycling tests are further performed, revealing 97.7% capacity retention at 1C after 100 cycles [Figure 3C and Supplementary Figure 5] and 95.2% retention at 10C after 1,500 cycles [Figure 3D], and the porous-microspherical morphology can mainly be retained during the cycling [Supplementary Figure 6]. This superior cyclic stability of $Nb_4W_7O_{31}$ is among the best results obtained from the reported anode materials with the intercalation characteristic [Supplementary Table 2].

To prove the practicability of $Nb_4W_7O_{31}$, it is coupled with a $LiFePO_4$ cathode, and the resultant full cell is studied. Its average working voltage is ~1.75 V [Figure 3E], matching well with the operating potentials of both $LiFePO_4$ [Supplementary Figure 7] and $Nb_4W_7O_{31}$. It exhibits a large reversible capacity of 200 mAh g^{-1} at 0.1C. The reversible capacity remains 180, 156, 110, and 87 mAh g^{-1} at 0.5C, 1C, 2C, and 5C, respectively [Figure 3F]. It remains at 136 mAh g^{-1} with high-capacity retention of 88.1% after 200 cycles at 1C [Figure 3G]. In addition, a bright LED bulb can be lit up by the full cell after enduring long-term cycling [Figure 3G]. Although the gravimetric energy density of $Nb_4W_7O_{31}$-based full cells is lower than that of traditional graphite-based full cells, $Nb_4W_7O_{31}$ owns several merits compared with graphite, including inherent safety performance, high rate capability, and good cyclic stability. Therefore, $Nb_4W_7O_{31}$ is a very promising anode material for safe, fast-charging, and long-life LIBs.

In order to know why $Nb_4W_7O_{31}$ owns comprehensively good electrochemical properties, several in-depth characterizations are conducted. The dQ/dV curves of the $Nb_4W_7O_{31}$/Li half cell in Figure 3H are deduced from its galvanostatic discharge-charge curves at 0.1C, revealing the redox mechanism of $Nb_4W_7O_{31}$. During the first cycle, there exist three peak pairs, respectively located at ~2.1/~2.2, ~1.5/~1.7, and ~1.1/~1.2 V. The first pair could be assigned to the redox reaction from the W^{6+}/W^{5+} redox couples, the second pair could be
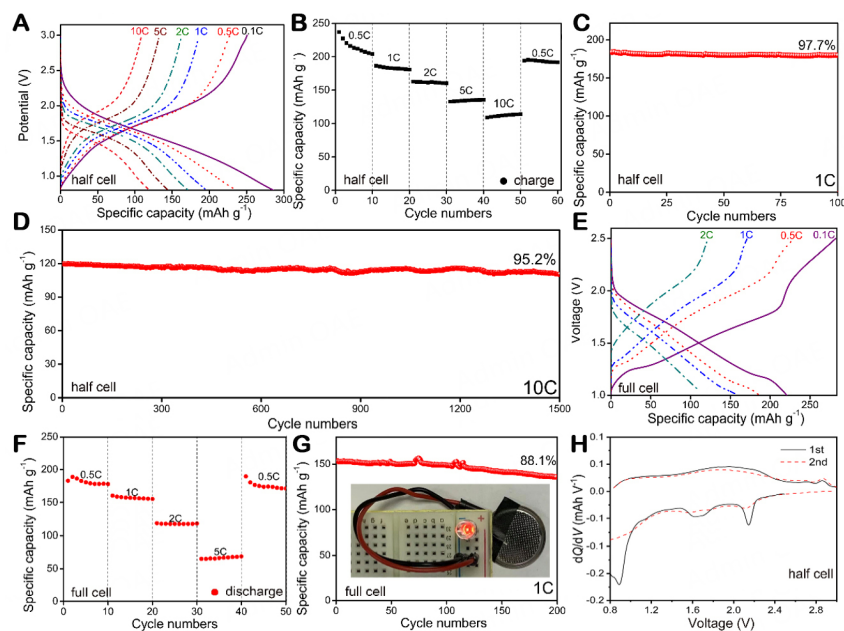
Figure 3. Electrochemical properties of $Nb_4W_7O_{31}$/Li half cell: (A) discharge/charge curves at various current rates, (B) rate capability, and cyclic stability at (C) 1C and (D) 10C (after rate-capability test). Electrochemical properties of $LiFePO_4$//$Nb_4W_7O_{31}$ full cell: (E) charge/discharge curves at various current rates, (F) rate capability, and (G) cyclic stability at 1C (after rate-capability test, *inset*: LED lit up by full cell). (H) dQ/dV curves of $Nb_4W_7O_{31}$/Li half cell at 0.1C.

assigned to the Nb^{5+}/Nb^{4+} couple, and the third pair could be rooted in the combination of Nb^{4+}/Nb^{3+} and W^{5+}/W^{4+} couples[35-37]. The subsequent sweep, however, is slightly different from the first one, which can be ascribed to the irreversible polarization, incomplete delithiation, and thin SEI-film formation during the first cycle[38]. The survey X-ray photoelectron spectroscopy (XPS) spectrum in Supplementary Figure 8 clearly shows the existence of Nb and W elements. Before discharge, the Nb-3d spectrum consists of a Nb-$3d_{5/2}$ (207.8 eV) and Nb-$3d_{3/2}$ (210.5 eV) doublet [Figure 4A][39], and the W-4f spectrum comprises a W-$4f_{7/2}$ (35.7 eV) and W-$4f_{5/2}$ (37.9 eV) doublet [Figure 4B][9], indicating the valences states of Nb and W are respectively +5 and +6, as expected. After discharged to 0.8 V, the lower doublet at 205.3 and 208.0 eV can correspond to Nb-$3d_{5/2}$ and Nb-$3d_{3/2}$ of Nb^{4+}, and the shoulder peak at 203.9 eV can be attributed to Nb^{3+}[40]; the W-4f spectrum can be well fitted by the characteristic peaks of W^{5+} and W^{4+}[41]. Therefore, the two electrons transfer in each Nb/W during the electrochemical reaction of $Nb_4W_7O_{31}$. Excitingly, after being charged to 3 V, the valence states of Nb and W almost fully recover +5 and +6, respectively, suggesting the excellent electrochemical reversibility of the multi-electron transfer in $Nb_4W_7O_{31}$. In addition, the electrochemical impedance spectroscopy (EIS) results of the $Nb_4W_7O_{31}$/Li half cell after different cycles show that the charge-transfer resistance gradually decreases with the increase of the cycle number and that the formed solid electrolyte interface (SEI) becomes stable after ten cycles [Supplementary Figure 9A-C].

To study the Li^+ diffusivity of $Nb_4W_7O_{31}$, its D_{Li} at various discharge/charge states are calculated from GITT data [Figure 5A] by using Equation (1)[42,43].

$$D_{Li} = \frac{4}{\pi\tau}\left(\frac{m_a V_m}{M_a S}\right)^2 \left(\frac{\Delta E_s}{\Delta E_\tau}\right)^2 \left(\tau \ll \frac{L^2}{D_{Li}}\right) \tag{1}$$

where m_a, M_a, V_m, S, and L present the mass, molar mass, molar volume, electrode surface area, and electrode thickness of $Nb_4W_7O_{31}$, respectively; τ is the time during which a constant current is applied; ΔE_s
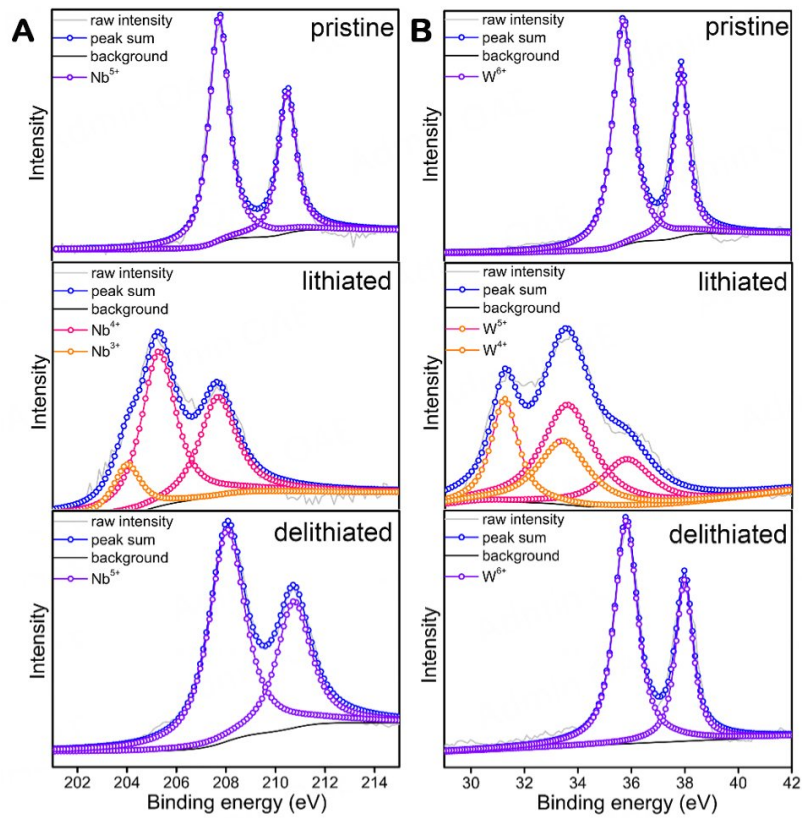
Figure 4. *Ex-situ* XPS spectra of pristine (OCV), lithiated (0.8 V), and delithiated (3.0 V) $Nb_4W_7O_{31}$ samples: (A) Nb-*3d* and (B) W-*4f*.
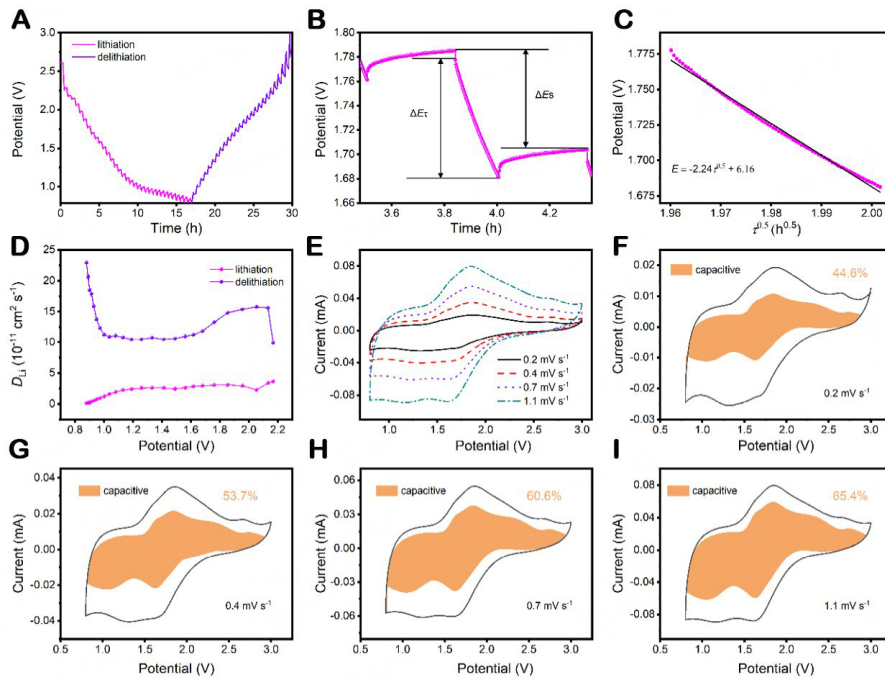
Figure 5. GITT characterization and intercalation-pseudocapacitive behavior of $Nb_4W_7O_{31}$: (A) first-cycle GITT curve at 0.1C, (B) *E vs. τ* curves for a single GITT step, (C) linear relationship of *E vs.τ*$^{0.5}$ during a typical titration, and (D) variations in Li^+ diffusion coefficients during lithiation and delithiation. (E) CV curves of $Nb_4W_7O_{31}$/Li half cell at various scan rates. Pseudocapacitive contributions at (F) 0.2, (G) 0.4, (H) 0.7, and (I) 1.1 mV s^{-1}.

and ΔE_τ respectively embody the change in the equilibrium potential and the change in potential during the current pulse, as presented in Figure 5B. This equation is reasonable and valid since the potential during each single titration can deliver a linear relationship with $\tau^{0.5}$ [Figure 5C]. The average D_{Li} value of $Nb_4W_7O_{31}$ during lithiation is 1.24×10^{-11} cm^2 s^{-1}, and that during delithiation is 1.09×10^{-10} cm^2 s^{-1} [Figure 5D]. The fact that the former value is obviously smaller than the latter one suggests that lithiation is the rate-determining step during the electrochemical reaction in $Nb_4W_7O_{31}$, which is similar to the cases in $Li_4Ti_5O_{12}$ and $TiNb_2O_7$[8,33]. The large D_{Li} value of $Nb_4W_7O_{31}$ is confirmed by the EIS method [Supplementary Figure 9D and E] and surpasses those of the previously reported niobate, vanadate, and titanate anode materials ($< 1 \times 10^{-11}$ cm^2 s^{-1}, Supplementary Table 3). Such fast Li$^+$ transport in $Nb_4W_7O_{31}$ is undoubtedly rooted in its criss-cross Li$^+$ transport network, allowing longitudinal transport along the large-sized pentagonal/quadrangular tunnels and transverse transport between the large-spaced MO_x (x = 6 and 7) layers.

For further understanding of the electrochemical kinetics of $Nb_4W_7O_{31}$, additional analyses are conducted based on the CV curves at various scan rates [Figure 5E], quantitatively determining the detailed contributions of the capacitive process (jv) and the diffusion-controlled process ($kv^{0.5}$) according to Equation (2)[44,45]:

$$I\,(V) = jv + kv^{0.5} \tag{2}$$

where I represents the detected current at a fixed potential, and j and k are adjustable factors. The resulting percentage of the capacitive contribution increases from 44.6% (0.2 mV s^{-1}, Figure 5F) to 53.7% (0.4 mV s^{-1}, Figure 5G), 60.6% (0.7 mV s^{-1}, Figure 5H), and 65.4% (1.1 mV s^{-1}, Figure 5I) with the scan-rate increasing. Therefore, this $Nb_4W_7O_{31}$ material reveals significant intercalation-pseudocapacitance behavior. This desirable behavior, the intrinsic charge-transport characteristic, and the extrinsic porous-microspherical morphology work together to achieve the superior rate capability of the $Nb_4W_7O_{31}$ material in this study.

To clarify the crystal-structural evolution of $Nb_4W_7O_{31}$ during lithiation/delithiation, an *in-situ* XRD experiment is carried out at 0.3C, as exhibited in Figure 6A and B. The weak WO_3 peaks located at 22.8, 23.7, 24.5, 33.8, and 34.5° do not shift during the electrochemical reaction, indicating that the tiny WO_3 impurity is inactive. The diffraction peaks initially located at 22.8, 23.2, 26.5, 28.1, 29.1, 30.3, 31.2, 33.0, and 35.1° correspond to the (001), (111), (270), (650), (800), (280), (660), (840), and (461) planes of $Nb_4W_7O_{31}$, respectively. During the first lithiation, these diffraction peaks show gradually decreased intensity and complicated shifts. From open-circuit voltage (OCV, ~2.7 V) to 1.8 V, they gradually shift to lower 2θ angles. Then, they suddenly shift to higher 2θ angles in a very short time. Finally, from 1.7 V to 0.8 V, they shift to lower 2θ angles again. During the subsequent delithiation, they monotonously shift to higher 2θ angles and almost recover their original intensities and positions at 3.0 V. This peak-evolution behavior confirms that only solid-solution reactions occur in the electrochemical process and suggests that the short and irreversible process at ~1.7 V during the first lithiation contributes to the small capacity loss [Figure 3A]. During the second lithiation, the peak evolution is almost contrary to that during both the first and second delithiation, demonstrating the intercalation-type nature of $Nb_4W_7O_{31}$ with superior structural and electrochemical reversibility after the first lithiation.

The lattice constants of $Nb_4W_7O_{31}$ at various discharge/charge states are calculated by a simple method. For the tetragonal structure, the interlayer spacing of the (280) plane is only associated with the lattice constant a, which can be calculated from the crystal and diffraction data by using Equation (3).

$$1/d^2 = h^2/a^2 + k^2/b^2 + l^2/c^2 \tag{3}$$
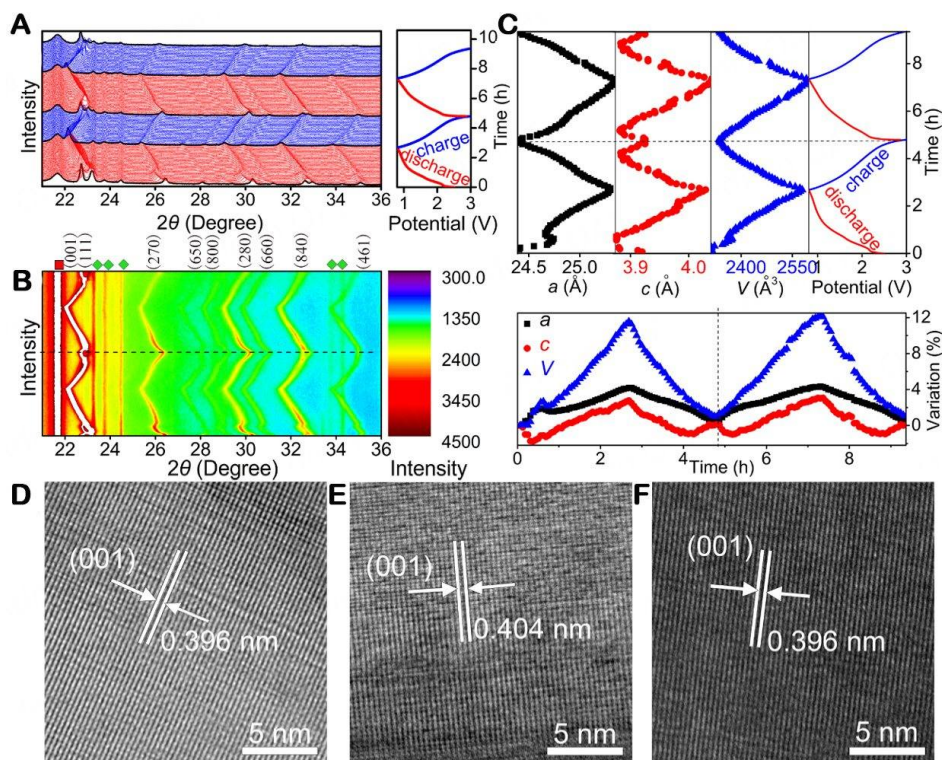
Figure 6. First two-cycle (A) pristine and (B) two-dimensional *in-situ* XRD patterns of $Nb_4W_7O_{31}$/Li *in-situ* cell with corresponding discharge/charge curves within 3.0-0.8 V at 0.3C (■: PE preservative film; ◆: WO_3). (C) Variations in lattice constants of $Nb_4W_7O_{31}$. *Ex-situ* HRTEM images of (D) pristine (OCV), (E) lithiated (0.8 V), and (F) delithiated (3.0 V) $Nb_4W_7O_{31}$ samples.

In this equation, (*hkl*) embodies the plane index (*h* = 2, *k* = 8, and *l* = 0 when calculating the *a* values), and *d* represents the interlayer spacing, which can be determined through Bragg's Law. The resultant *a*-variation is revealed in Figure 6C and Supplementary Table 4. When Li^+ ions gradually insert into the $Nb_4W_7O_{31}$ lattice, the *a*-variation follows a sequence of slight increase → tiny decrease → small increase. When Li^+ ions are gradually extracted from the lattice, the *a* value monotonously decreases, which is highly reversible in the second cycle. This *a*-variation behavior matches well with the (270), (650), (800), (280), (660), and (840) peak shifts. The maximum *a*-value change is only +4.1% at 0.8 V. Similarly, the interlayer spacing of the (461) plane is only associated with *a* and *c*. Since the *a* values have been obtained, the *c* values can be easily achieved also using Equation (3). The *c* evolution follows a sequence of slight decrease → small increase with the maximum change of only +2.7% during lithiation and is highly reversible during delithiation [Figure 6C and Supplementary Table 4]. This slight and reversible *c* variation is confirmed by the *ex-situ* high-resolution transmission electron microscopy (HRTEM) characterization, showing that the (001) interlayer spacing enlarges from ~0.395 nm (OCV, Figure 6D) to ~0.404 nm (0.8 V, Figure 6E) and fully recovers (3.0 V, Figure 6F). The maximum *V*-value change, which only links to the *a* and *c* changes, is +11.2%. This percentage is similar to those of graphite (+13.2%) and $Mo_3Nb_{14}O_{44}$ (+10.6%) with similar layered structures [Supplementary Table 5][46,47]. The volume increase of graphite and $Mo_3Nb_{14}O_{44}$ is mainly caused by the interlayer expansion (+10.2% for graphite and +9.9% for $Mo_3Nb_{14}O_{44}$)[45,46]. In sharp contrast, the interlayer expansion along the *c* direction in $Nb_4W_7O_{31}$ is only 2.7%, and the expansion along the *a* and *b* directions (4.1%) also contributes to its moderate volume increase. Compared with the one-dimensionally considerable expansion in graphite and $Mo_3Nb_{14}O_{44}$, the three-dimensionally uniform and small expansion in $Nb_4W_7O_{31}$ can more effectively alleviate the damage of volume expansion, greatly benefiting the structural and cyclic stability.
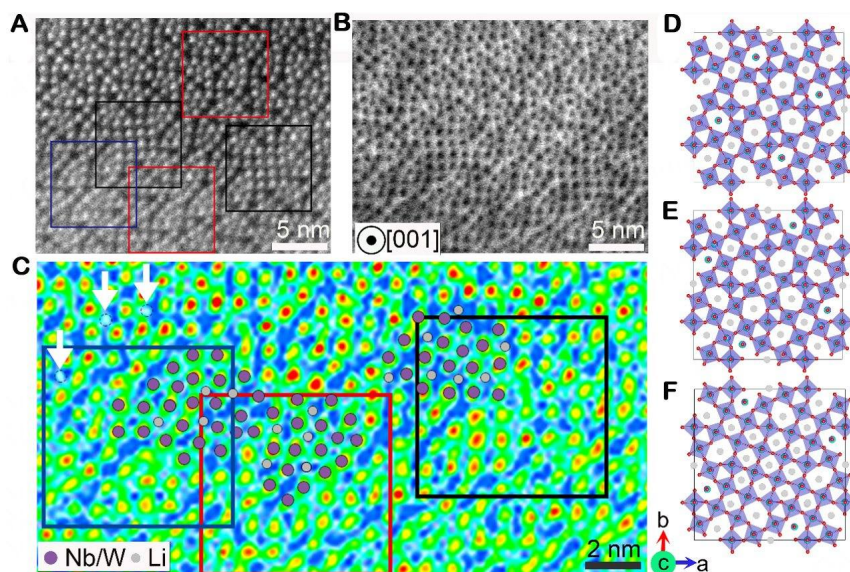
Figure 7. HAADF and ABF STEM results of lithiated $Nb_4W_7O_{31}$ (0.8 V) confirming its Li^+-storage sites: (A) atomic-resolution HAADF-STEM and (B) ABF-STEM images viewed along [001], (C) magnified ABF-STEM color image with inverted image contrast showing the positions of inserted Li^+ ions (some examples are indicated by dotted circles and highlighted by white arrows). Unit cells corresponding to Structure A, Structure B, and Structure C are respectively highlighted by red, blue, and black squares in (A and C). For clarity, in (C), Nb/W and Li are shown in only one-quarter of each unit cell due to the symmetry of the *P4* space group. Crystal structure models of (D) lithiated Structure A, (E) lithiated Structure B, and (F) lithiated Structure C corresponding to HAADF-STEM and ABF-STEM images.

To reveal the real crystal structure of $Nb_4W_7O_{31}$ and its Li^+-storage sites after lithiation, spherical-aberration-corrected STEM is employed. The high-angle annular dark field (HAADF, Figure 7A) and the annular bright field (ABF, Figure 7B) STEM images of lithiated $Nb_4W_7O_{31}$ (at 0.8 V) can be viewed along the [001] zone axis, which are acquired under optimal imaging conditions for identifying heavy atoms (Nb and W) and light atoms (Li and O), respectively[48]. The *a* value obtained from the STEM images is 25.30 Å, in good agreement with the *in-situ* XRD results. Since $Nb_4W_7O_{31}$ is an intercalation-type Li^+-storage material with small expansion along all three dimensions, the $Nb_4W_7O_{31}$ framework should be well-kept during repeated lithiation/delithiation. Consequently, the HAADF-STEM image containing the exact positions of Nb and W can reflect the real structure of $Nb_4W_7O_{31}$. In Figure 7A, the intergrowth of Structure A, Structure B, and Structure C with different orientations and some defects can be observed, confirming the structural mixing in $Nb_4W_7O_{31}$, which can be the main cause of the three-dimensionally uniform and small expansion/shrinkage. In order to intuitively identify the light-atom positions, inverted image contrast with colors is applied for the magnified ABF-STEM image [Figure 7C]. As a result, the inserted Li^+ ions can be seen, and some examples are indicated by dotted circles and highlighted by the white arrows. Clearly, the inserted Li^+ ions occupy the pentagonal and quadrangular tunnels in the three structures, as schematically illustrated in Figure 7D-F.

CONCLUSIONS

Porous $Nb_4W_7O_{31}$ microspheres formed by self-assembly of nanorods are developed as a new intercalation-type anode material with comprehensively good Li^+-storage properties. The presence of proper surfactants during the solvothermal process is the key to forming this hierarchical morphology. $Nb_4W_7O_{31}$ owns an interesting crystal structure with mixed TTB and confined ReO_3 units, abundant large-sized tunnels, and a large interlayer spacing (~3.95 Å), resulting in the three-dimensionally uniform expansion/shrinkage (≤ 4.1%) and fast Li^+ transport (1.24 × 10^{-11} cm^2 s^{-1} during lithiation and 1.09 × 10^{-10} cm^2 s^{-1} during delithiation) when the external Li^+ ions insert into/extract from the pentagonal and quadrangular tunnels.

These structural merits combined with the morphological merits enable excellent cyclic stability (95.2% capacity retention after 1,500 cycles at 10C) and superior rate capability (10C *vs.* 0.1C capacity retention percentage of 47.6%). The highly reversible redox reactions of the multiple Nb^{5+}/Nb^{4+}, Nb^{4+}/Nb^{3+}, W^{6+}/W^{5+}, and W^{5+}/W^{4+} couples in $Nb_4W_7O_{31}$ are confirmed and enable the large reversible capacity (252 mAh g^{-1} at 0.1C), safe operating potential (~1.66 V), and high first-cycle Coulombic efficiency (88.4%). Additionally, the $LiFePO_4$//$Nb_4W_7O_{31}$ full cell also exhibits prominent electrochemical properties, demonstrating the practicability of the porous $Nb_4W_7O_{31}$ microspheres for high-performance LIBs. The structural and morphological designs in this work can find its extensional applications for enhancing the electrochemical properties of other energy-storage materials.

DECLARATIONS

Authors' contributions
Made substantial contributions to the conception and design of the study: Lin C
Performed data analysis and interpretation: Jin X, Yuan Q, Sun X
Performed data acquisition: Jin X, Yuan Q
Provided administrative, technical, and material support: Lin C, Wu J, Liu X

Availability of data and materials
Not applicable.

Financial support and sponsorship
None.

Conflicts of interest
All authors declared that there are no conflicts of interest.

Ethical approval and consent to participate
Not applicable.

Consent for publication
Not applicable.

Copyright
© The Author(s) 2024.

REFERENCES

1.   Wang L, Liu T, Wu T, Lu J. Strain-retardant coherent perovskite phase stabilized Ni-rich cathode. *Nature* 2022;611:61-7. DOI
2.   Wang CY, Liu T, Yang XG, et al. Fast charging of energy-dense lithium-ion batteries. *Nature* 2022;611:485-90. DOI
3.   Liu T, Liu J, Li L, et al. Origin of structural degradation in Li-rich layered oxide cathode. *Nature* 2022;606:305-12. DOI
4.   Zhang W, Seo DH, Chen T, et al. Kinetic pathways of ionic transport in fast-charging lithium titanate. *Science* 2020;367:1030-4. DOI
5.   Griffith KJ, Wiaderek KM, Cibin G, Marbella LE, Grey CP. Niobium tungsten oxides for high-rate lithium-ion energy storage. *Nature* 2018;559:556-63. DOI PubMed
6.   Aravindan V, Gnanaraj J, Lee YS, Madhavi S. Insertion-type electrodes for nonaqueous Li-ion capacitors. *Chem Rev* 2014;114:11619-35. DOI PubMed
7.   Sivakkumar SR, Nerkar JY, Pandolfo AG. Rate capability of graphite materials as negative electrodes in lithium-ion capacitors. *Electrochim Acta* 2010;55:3330-5. DOI
8.   Zhao B, Ran R, Liu M, Shao Z. A comprehensive review of $Li_4Ti_5O_{12}$-based electrodes for lithium-ion batteries: the latest advancements and future perspectives. *Mater Sci Eng R Rep* 2015;98:1-71. DOI
9.   Yan L, Shu J, Li C, et al. $W_3Nb_{14}O_{44}$ nanowires: ultrastable lithium storage anode materials for advanced rechargeable batteries. *Energy Stor Mater* 2019;16:535-44. DOI
10. Yan L, Cheng X, Yu H, et al. Ultrathin $W_9Nb_8O_{47}$ nanofibers modified with thermal NH_3 for superior electrochemical energy storage.

Energy Stor Mater 2018;14:159-68. DOI

11.   Yan L, Lan H, Yu H, et al. Electrospun $WNb_{12}O_{33}$ nanowires: superior lithium storage capability and their working mechanism. *J Mater Chem A* 2017;5:8972-80. DOI

12.   Griffith KJ, Grey CP. Superionic lithium intercalation through 2×2 nm^2 columns in the crystallographic shear phase $Nb_{18}W_8O_{69}$. *Chem Mater* 2020;32:3860-8. DOI

13.   Yang Y, Zhu H, Xiao J, et al. Achieving ultrahigh-rate and high-safety Li^+ storage based on interconnected tunnel structure in micro-size niobium tungsten oxides. *Adv Mater* 2020;32:e1905295. DOI

14.   Yang Y, Zhao J. Wadsley-roth crystallographic shear structure niobium-based oxides: promising anode materials for high-safety lithium-ion batteries. *Adv Sci* 2021;8:e2004855. DOI PubMed PMC

15.   Kim Y, Jacquet Q, Griffith KJ, et al. High rate lithium ion battery with niobium tungsten oxide anode. *J Electrochem Soc* 2021;168:010525. DOI

16.   Marinder BO. The pentagonal column and the ReO_3-type structure. *Angew Chem Int Ed* 1986;25:431-42. DOI

17.   Bryntse I. A bismuth niobium oxide, $BiNb_{5.4}O_{15}$, with a TTB-related structure. *Acta Chem Scand* 1993;47:789-92. DOI

18.   Stephenson NC. A structural investigation of some stable phases in the region $Nb_2O_5.WO_3$-WO_3. *Acta Crystallogr B* 1968;24:637-53. DOI

19.   Iijima S, Allpress JG. Structural studies by high-resolution electron microscopy: tetragonal tungsten bronze-type structures in the system Nb_2O_5-WO_3. *Acta Crystallogr A* 1974;30:22-9. DOI

20.   Toby BH. *EXPGUI*, a graphical user interface for *GSAS*. *J Appl Cryst* 2001;34:210-3. DOI

21.   Larson AC, Von Dreele RB, General structure analysis system (GSAS). Los Alamos national laboratory report LAUR 86-748; 2004. Available from: https://11bm.xray.aps.anl.gov/documents/GSASManual.pdf [Last accessed on 4 Jan 2024].

22.   Li X, Lin H, Li J, Wang N, Lin C, Zhang L. Chemical sintering of graded TiO_2 film at low-temperature for flexible dye-sensitized solar cells. *J Photochem Photobiol A* 2008;195:247-53. DOI

23.   Fu Q, Li R, Zhu X, et al. Design, synthesis and lithium-ion storage capability of $Al_{0.5}Nb_{24.5}O_{62}$. *J Mater Chem A* 2019;7:19862-71. DOI

24.   Zhu X, Xu J, Luo Y, et al. $MoNb_{12}O_{33}$ as a new anode material for high-capacity, safe, rapid and durable Li^+ storage: structural characteristics, electrochemical properties and working mechanisms. *J Mater Chem A* 2019;7:6522-32. DOI

25.   Zhu X, Fu Q, Tang L, et al. $Mg_2Nb_{34}O_{87}$ porous microspheres for use in high-energy, safe, fast-charging, and stable lithium-ion batteries. *ACS Appl Mater Interfaces* 2018;10:23711-20. DOI

26.   Lin C, Deng S, Kautz DJ, et al. Intercalating $Ti_2Nb_{14}O_{39}$ anode materials for fast-charging, high-capacity and safe lithium-ion batteries. *Small* 2017;13:1702903. DOI

27.   Yang C, Deng S, Lin C, et al. Porous $TiNb_{24}O_{62}$ microspheres as high-performance anode materials for lithium-ion batteries of electric vehicles. *Nanoscale* 2016;8:18792-9. DOI

28.   Tahir MN, Theato P, Oberle P, et al. Facile synthesis and characterization of functionalized, monocrystalline rutile TiO_2 nanorods. *Langmuir* 2006;22:5209-12. DOI

29.   Sarfraz S, Ali S, Khan SA, et al. Phase diagram and surface adsorption behavior of benzyl dimethyl hexadecyl ammonium bromide in a binary surfactant-water system. *J Mol Liq* 2019;285:403-7. DOI

30.   Bai P, Su F, Wu P, et al. Copolymer-controlled homogeneous precipitation for the synthesis of porous microfibers of alumina. *Langmuir* 2007;23:4599-605. DOI

31.   Jiang C, Hosono E, Ichihara M, Honma I, Zhou H. Synthesis of nanocrystalline $Li_4Ti_5O_{12}$ by chemical lithiation of anatase nanocrystals and postannealing. *J Electrochem Soc* 2008;155:A553. DOI

32.   Penn RL, Banfield JF. Imperfect oriented attachment: dislocation generation in defect-free nanocrystals. *Science* 1998;281:969-71. DOI PubMed

33.   Guo B, Yu X, Sun XG, et al. A long-life lithium-ion battery with a highly porous $TiNb_2O_7$ anode for large-scale electrical energy storage. *Energy Environ Sci* 2014;7:2220-6. DOI

34.   Fu Q, Zhu X, Li R, et al. A low-strain $V_3Nb_{17}O_{50}$ anode compound for superior Li^+ storage. *Energy Stor Mater* 2020;30:401-11. DOI

35.   Wang X, Shen G. Intercalation pseudo-capacitive $TiNb_2O_7$@carbon electrode for high-performance lithium ion hybrid electrochemical supercapacitors with ultrahigh energy density. *Nano Energy* 2015;15:104-15. DOI

36.   Yang L, Zhu X, Li X, et al. Conductive copper niobate: superior Li^+-storage capability and novel Li^+-transport mechanism. *Adv Energy Mater* 2019;9:1902174. DOI

37.   Ye W, Yu H, Cheng X, et al. Highly efficient lithium container based on non-Wadsley-Roth structure $Nb_{18}W_{16}O_{93}$ nanowires for electrochemical energy storage. *Electrochim Acta* 2018;292:331-8. DOI

38.   Qian S, Yu H, Yan L, et al. High-rate long-life pored nanoribbon VNb_9O_{25} built by interconnected ultrafine nanoparticles as anode for lithium-ion batteries. *ACS Appl Mater Interfaces* 2017;9:30608-16. DOI

39.   Fu Q, Liu X, Hou J, et al. Highly conductive $CrNb_{11}O_{29}$ nanorods for use in high-energy, safe, fast-charging and stable lithium-ion batteries. *J Power Sources* 2018;397:231-9. DOI

40.   Zhu H, Cheng X, Yu H, et al. $K_6Nb_{10.8}O_{30}$ groove nanobelts as high performance lithium-ion battery anode towards long-life energy storage. *Nano Energy* 2018;52:192-202. DOI

41.   Sarma DD, Rao CNR. XPES studies of oxides of second- and third-row transition metals including rare earths. *J Electron Spectrosc*

Relat Phenom 1980;20:25-45. DOI

42. Bard AJ, Faulkner LR. Electrochemical methods: fundamentals and applications, 2nd edition. New York: Wiley; 2000. Available from: https://www.wiley.com/en-us/Electrochemical+Methods:+Fundamentals+and+Applications,+2nd+Edition-p-9780471043720 [Last accessed on 16 Nov 2023]

43. Zhu X, Cao H, Li R, et al. Zinc niobate materials: crystal structures, energy-storage capabilities and working mechanisms. *J Mater Chem A* 2019;7:25537-47. DOI

44. Augustyn V, Simon P, Dunn B. Pseudocapacitive oxide materials for high-rate electrochemical energy storage. *Energy Environ Sci* 2014;7:1597-614. DOI

45. Augustyn V, Come J, Lowe MA, et al. High-rate electrochemical energy storage through Li^+ intercalation pseudocapacitance. *Nat Mater* 2013;12:518-22. DOI

46. Schweidler S, de Biasi L, Schiele A, Hartmann P, Brezesinski T, Janek J. Volume changes of graphite anodes revisited: a combined *Operando* X-ray diffraction and *in situ* pressure analysis study. *J Phys Chem C* 2018;122:8829-35. DOI

47. Li R, Liang G, Zhu X, et al. $Mo_3Nb_{14}O_{44}$: a new Li^+ container for high-performance electrochemical energy storage. *Energy Environ Mater* 2021;4:65-71. DOI

48. Gu L, Zhu C, Li H, et al. Direct observation of lithium staging in partially delithiated $LiFePO_4$ at atomic resolution. *J Am Chem Soc* 2011;133:4661-3. DOI